Commissioning of the imaging neutral particle analyser for the ASDEX Upgrade tokamak

OPEN ACCESS
IOP Publishing
Plasma Physics and Controlled Fusion
Plasma Phys. Control. Fusion **66** (2024) 035008 (15pp)
https://doi.org/10.1088/1361-6587/ad1ec1

Commissioning of the imaging neutral particle analyser for the ASDEX Upgrade tokamak

J Rueda-Rueda[1,*], M Garcia-Munoz[1], E Viezzer[1], P A Schneider[2], J Garcia-Dominguez[1], P Oyola[1], J Galdon-Quiroga[1], J Hidalgo-Salaverri[3], X Du[4], M A Van Zeeland[4], M Videla-Trevin[5], A Jansen van Vuuren[1] and ASDEX Upgrade Team[6]

[1] Department of Atomic, Molecular and Nuclear Physics, University of Seville, Seville, Spain
[2] Max Planck Institute for Plasma Physics, Boltzmannstr. 2, 85748 Garching, Germany
[3] Department of Mechanic and Manufacturing Engineering, University of Seville, Seville, Spain
[4] General Atomics, San Diego, CA 92186-5608, United States of America
[5] Department of Materials and Transport Science and Engineering, University of Seville, Seville, Spain

E-mail: jrrueda@us.es

Received 23 August 2023, revised 30 December 2023
Accepted for publication 15 January 2024
Published 1 February 2024

Abstract

An imaging neutral particle analyser (INPA) diagnostic has been installed and commissioned at the ASDEX Upgrade (AUG) tokamak. The AUG INPA diagnostic provides energy and radially resolved measurements of the fast-ion (FI) distribution, complementing the existing set of diagnostic which measure the confined FI population. To this end, it analyses charge exchange (CX) neutrals produced in reactions between FI and neutrals injected by a neutral beam injector. These CX neutrals are ionised by a 20 nm carbon foil and deflected towards a scintillator by the machine magnetic field. The use of a scintillator as active component allows us to cover the whole plasma radial range with an energy resolution of 9 keV and a spatial of 3 cm for 93 keV deuterons. First measurements demonstrate the high sensitivity of the INPA diagnostic to different AUG fast-ion distribution functions, from NBI and ion-cyclotron resonance heating origin, and show good agreement with the synthetic diagnostic.

Keywords: fast-ion diagnosis, neutral particle analyser, scintillator diagnostics

1. Introduction

Fast ions (FI) are a key source of energy and momentum to ensure fusion performance in future fusion reactors [1]. The redistribution of these particles, caused by their interaction with magnetohydrodynamic (MHD) instabilities, are a known cause of degradation of current drive and heating [2–4] and their losses can severely damage the plasma facing components [5, 6]. The interaction of FI with these instabilities is known to occur in localised regions of the phase-space [7, 8]; hence, assessing the FI distribution in phase space with good spatial and temporal resolution is essential to develop new control techniques. For this purpose, new diagnostics techniques to measure the confined FI population in phase space with fast temporal response and high resolution in phase space are needed. We hereby report on the commissioning of such a new FI diagnostic, an imaging neutral particle analyser (INPA) installed in the ASDEX Upgrade (AUG) tokamak [9, 10]. This diagnostic provides energy-resolved FI profiles,

[6] See Stroth *et al* 2022 (https://doi.org/10.1088/1741-4326/ac207f) for the ASDEX Upgrade Team.
[*] Author to whom any correspondence should be addressed.

complementing the state-of-the-art suite of FI diagnostics installed in AUG; among which fast-ion loss detector (FILD) [11], neutron detectors [12], fast-ion D-α (FIDA) [13], neutral particle analysers (NPAs) [14], ion cyclotron emission (ICE) diagnostics [15] and collective Thomson scattering [16] out-stand.

Both FIDA and NPAs are based on charge exchange reactions (CX); where an electron is transferred from an ion to a neutral, with no significant energy nor momentum exchange [17, 18], so the neutral created after the electron transfer essentially keeps the velocity of the old ion. NPAs analyse directly the escaping neutral while FIDA relies on the de-excitation photon it emits. Traditional NPAs employs analysers installed out-vessel connected via a vacuum channel to the main plasma volume [19]. This imposes the limitation of having a constrained field-of-view (FoV). The INPA diagnostic overcomes this limitation having the analyser system installed inside the tokamak; hence, the whole radial range can be accessed. To this ends, it combines the use of an ultra-thin carbon foil and scintillator plates [20, 21]. CX neutrals are ionised in-vessel by the carbon foil (20 nm in the AUG setup) and deflected into a scintillator by the local magnetic field. The strike position of the scintillator is directly related to the energy and pitch angle of the CX neutral. The birth location of the CX neutrals is mainly localised along the NBI path, as the overlap of fast-ion distribution and neutral density is not significant elsewhere. This is due to the low concentration of background neutrals within the core region, and the low density of fast ions at the edge, where the background neutral concentration is large, as reported for FIDA studies at AUG [13]. This allows to establish a relation, via modelling, between the measured pitch angle and the radial birth location of the CX particle, as detailed in [9].

In this paper, the first measurements of the recently installed INPA diagnostic at AUG are reported, demonstrating its capability to measure the most common FI distribution which can be generated in AUG and its potential to shed light on the FI redistribution. Section 2 presents briefly the setup and installation of the AUG INPA. In section 3 we introduce the characterisation of the diagnostic while section 4 focuses on the first experimental signals. Finally, the upgraded synthetic diagnostic is presented and compared against experimental results. The design and the installation was already presented in [9, 10]. The reader is referred to those publications for a detailed description of the mechanical system and the design process.

2. INPA diagnostic setup at ASDEX Upgrade

AUG is equipped with eight NBI sources, grouped in two NBI boxes, providing up to 20 MW. Box 1 (sources #1–#4) has a maximum energy of 60 keV while box 2 (sources #5–#8) of 93 keV, for deuterium. The INPA diagnostic is placed such that its field of view aligns with NBI#3 (the main diagnostic beam at AUG), as depicted in figure 1.

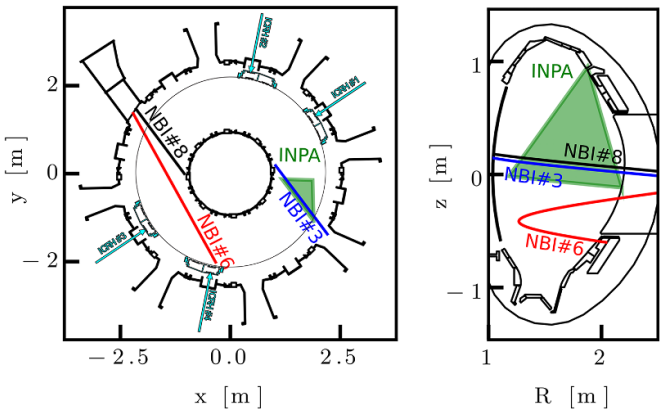

Figure 1. Toroidal and poloidal cross-sections of the AUG tokamak. Solid lines represent the NBI injection direction while the shaded area represents the INPA field of view.

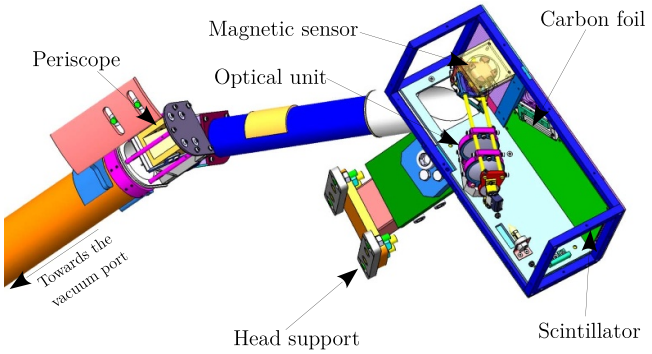

Figure 2. Overview of the INPA in-vessel mechanical design. Walls of the detector head as well as the periscope are removed to show the internal components.

The INPA diagnostic is composed of three main elements: the detector head, the optical system and the out-vessel acquisition systems. The detector head, shown in figure 2, is located in the upper part of sector 16, at the low-field-side of AUG and contains the scintillator plate together with the carbon foil and the first optical components. The particles are ionised by the ultra-thin carbon foil inside the head and deflected onto the scintillator, where light is emitted. Then, the rest of the optical system, composed by 4 mirrors and 4 lenses, guides this light to the acquisition system. A high-resolution camera to obtain the image of the scintillator plate, installed just outside the tokamak vessel. The size of the scintillator allows us to cover from 12 to 160 keV (for deuterium ions and an equilibrium field of -2.5 T on axis) and from R $=$ 1.55 m to the outer separatrix.

As for other NPA systems, the flux of CX neutrals entering the detector head can be directly related with the fast-ion distribution [18]. It can be written as the convolution of the fast-ion density with the source of neutral particles, weighted by the CX reaction cross-section and the attenuation along the LOS:

$$\Phi = \int_{V_0} \mathrm{d}\vec{r} \int \mathrm{d}\vec{v}_F \int \mathrm{d}\vec{v}_n \sigma_{CX}\left(v_{rel}\right) v_{rel} f\left(\vec{v}_F, \vec{r}\right) \cdot n_n\left(\vec{v}_n, \vec{r}\right) e^{-\frac{|\vec{r}-\vec{r}_p|}{d_0\left(\vec{r},\vec{v}_n\right)}} \quad (1)$$

where the subindex F refers to the fast ions, n to the neutral particles, σ_{CX} is the charge-exchange cross section, v_{rel} the relative velocity between the FI and the neutral and $f(\vec{v}_F, \vec{r})$ is the fast-ion distribution function, $n_n(\vec{v}_n, \vec{r})$ the neutral distribution, $\vec{r}_p$ the detector pinhole position $d_0(\vec{r}, \vec{v}_n)$ the mean free path of the produced CX neutrals. The integration in real space is limited to the detector field-of-view, V_0. Note that the integrand is proportional to the neutral density. We can distinguish three populations of neutrals:

$$n_n = n_{\mathrm{NBI}} + n_{\mathrm{Halo}} + n_{\mathrm{Thermal}} \quad (2)$$

where n_{NBI} represents the neutral particles injected by the NBI, n_{Halo} the halo neutrals and n_{Thermal} stands for the the rest of neutral particles present in the plasma, for example, those released by the wall. The halo neutrals are a cloud of neutrals originated from CX reactions between the NBI neutrals and the thermal ions [22]. This cloud of neutrals is shifted towards the direction of plasma rotation. Therefore, the signal can be divided into three contributions: the one coming from the interaction of FI with the NBI neutrals, the one coming from the interaction of FI with the halo neutrals and the one coming from the interaction with the thermal neutrals. The contributions from NBI and halo are termed *active* while the thermal is termed *passive*. These contributions are shown in figure 3. The simulation was performed for a core plasma electron density of $n_e(0) = 4.5 \cdot 10^{19}$ m^{-3}, in line typical FI experiments at the AUG tokamak and a background neutral density which a maximum of 10^{15} m^{-3} at the plasma edge, also in line with previous FI studies [23]. The NBI fast-ion distribution was calculated with TRANSP [24, 25] and corresponds to a 59 keV on-axis source, it can be observed in figure 3(a). The complete synthetic signal is depicted in subplot (b). As depicted in figure 3(c), the halo contribution turns out to dominate in the plasma core and is wider than the NBI contribution while the passive contribution is well below the active level and is apparently distributed along all the possible radii (the relation between pitch and radial position can only be accurately established for CX neutrals originated along the NBI line [9]). For the case of the signal per units of energy, depicted in figure 3(d), the contribution is dominated by the active component at high energy, while the passive signal becomes significant at low energy, as neutrals coming from the edge suffer almost no attenuation due to reionisation.

The AUG-NBI setup together with the collimator geometry and optical resolution provide a radial resolution <3 cm (see section 5.1 for full details and calculation) and an energy resolution <9.5 keV (see section 3.4 for full details and calculation). Due to the energy-dependent nature of CX and reionisation reaction rates, the ionisation likelihood on the carbon foil, scintillator emission, and the radial distribution of the active source of neutrals (NBI), the INPA will not exhibit uniform

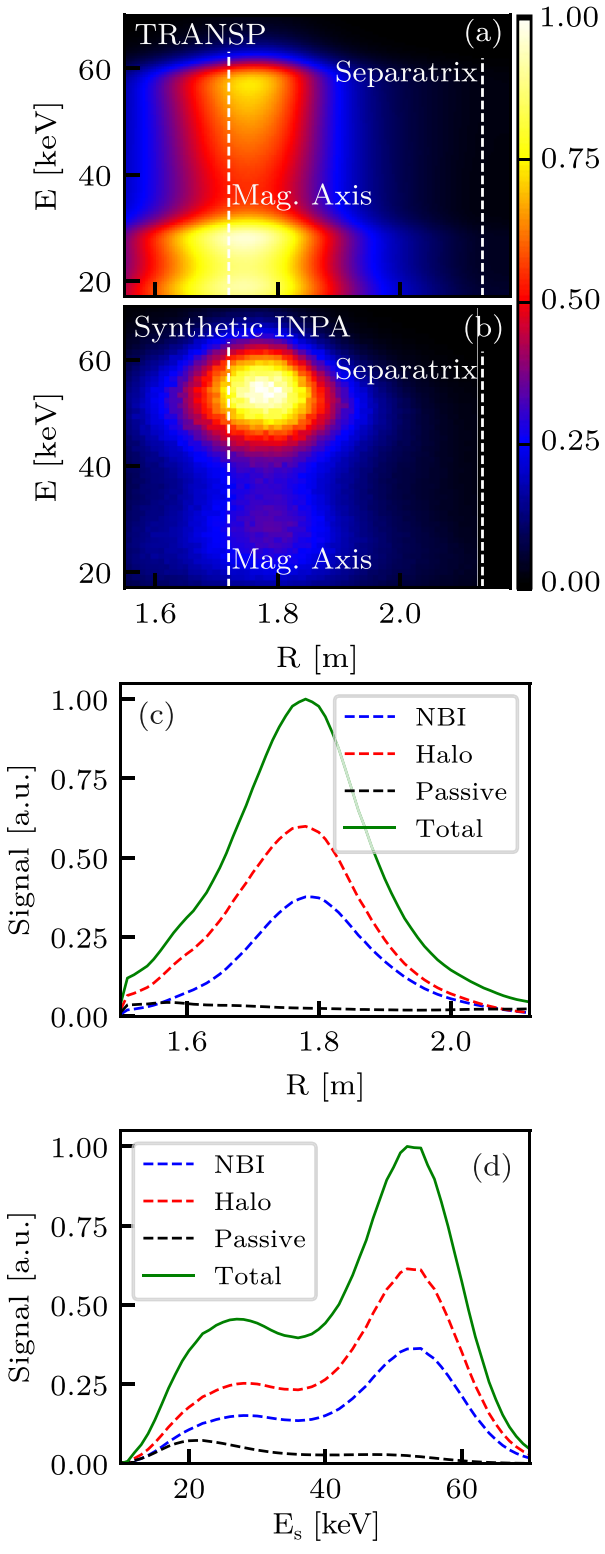

Figure 3. Example of synthetic signal for the AUG INPA diagnostic. (a) TRANSP fast-ion distribution function, integrated in pitch angle and z coordinates. (b) Synthetic camera frame remapped in energy and radius. (c) Contributions to the signal per unit of radius, as reconstructed in the INPA scintillator. The legend indicates the population of neutrals with which the fat ion has interacted to produce the CX neutral. (d) Contributions to the signal per unit of energy, also as reconstructed in the scintillator. E_s represents the energy of the particle impinging in the scintillator.

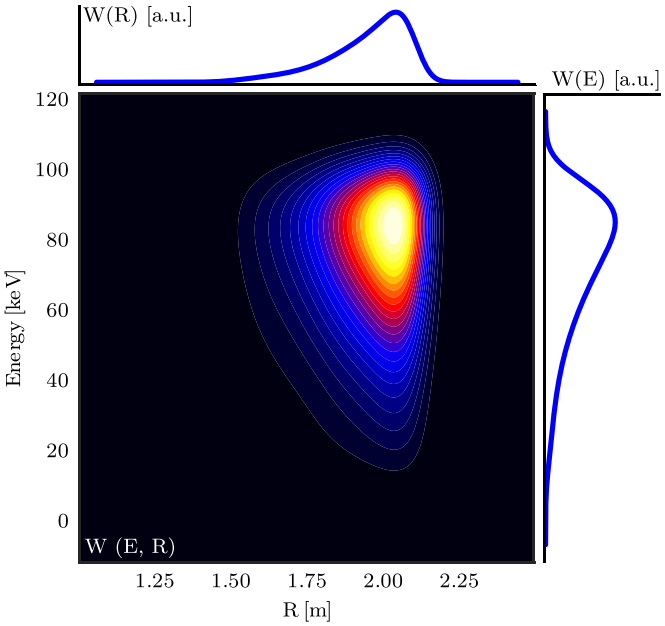

Figure 4. INPA sensitivity as function of FI energy and position.

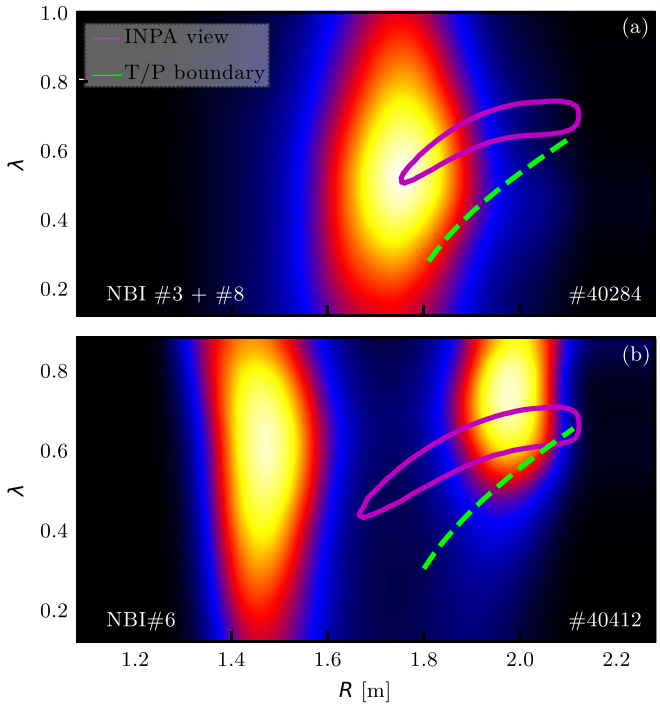

Figure 5. Pitch explored by the AUG INPA. (a) Example of on-axis NBI distribution. FI slowing down distribution calculated by TRANSP for a case where NBI#3 and #8 were active. The distribution was integrated in energy and in z around the midplane. The magenta line indicates the 10% level of the INPA view. The green line represents the estimation of the trapped/passing boundary. (b) Equivalent to (a) but for the a situation where only NBI#6 was active.

sensitivity across all points in phase space; meaning that not all volumes of the phase space will contribute equally to the INPA signal. The likelihood of a phase space volume to contribute to the INPA signal, the so-called diagnostic sensitivity or instrument function, is depicted in figure 4 for a typical plasma density for FI studies at AUG ($n_e(0) = 4.5 \cdot 10^{19}$ m^{-3}). The radial distribution of this instrument response, depicted in the upper subplot of figure 4, will be mainly given by the NBI deposition and halo profiles and the attenuation suffered by CX neutrals due to re-ionisation along their way towards the detector. The energy distribution of the instrument response, shown in the right subplot of figure 4, will also be affected by this attenuation, as low energy neutrals are more pronier to be re-ionised. In addition, to the CX cross sections, which decays with energy and scintillator emission (yield), which increases with energy. This energy response has a maximum at around 80 keV, as result of the competition between the CX cross section, the re-ionization along the LOS, the ionisation efficiency of the carbon foil and the scintillator yield. A deep analysis of how this instrument response scales with plasma parameters and on its calculations is out of the scope of this work and will be presented in a future publication together with the first tomographic reconstructions of AUG INPA signals.

As the measured particles are fast neutrals, the range of pitch ($\lambda = -v_\parallel/v$, $v_\parallel$ being the projection of the particle velocity along the magnetic field) which can be explored at each location is determined by the geometry of the field of view in combination with the magnetic equilibrium (see [9] for a full description). This range of pitch is relatively narrow ($\sim\pm 0.045$), so the geometry was optimised trying to overlap as much as possible with the FI distribution function created by the on- and off-axis NBI injection. An example of the explored pitch range and its comparison with two typical AUG FI distributions can be seen in figure 5. This figure shows the pitch explored by the INPA diagnostic together with the objective fast-ion distribution functions and the trapped-passing boundary, λ_b, estimated as:

$$\lambda_b(R) = \sqrt{1 - \frac{R_{\min}}{R}} \tag{3}$$

where $R_{\min}$ is the minimum radius of the magnetic flux surface. Notice that the AUG INPA will be mainly sensitive to passing ions.

3. Detector characterisation

3.1. Background noise

There are two sources of background noise which can affect the diagnostic signal: the noise from the acquisition system (read-out noise and dark current in the case of the camera) and plasma light which could enter through the pinhole and the holes in the optical head required for out-gassing. Other sources of noise, such as neutrons or electrons that can induce spurious scintillation are neglected. This can be bound to be reasonable as e^- and neutrons do not contribute significantly to the noise in similar diagnostics such as AUG FILDs, which share the same scintillator material. The origin of the camera noise is mainly thermal, and can be characterised using the

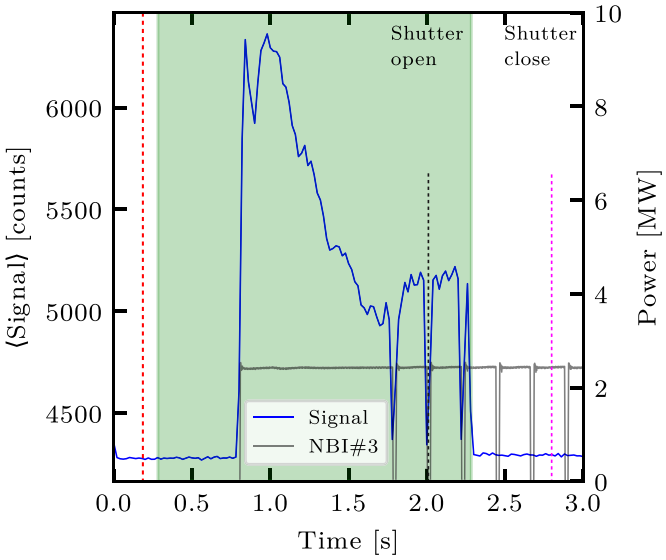

Figure 6. Mean number of counts in the whole INPA signal during discharge #40259. Green shaded area represents the period where the INPA shutter is open. Vertical dashed lines represent the time points referenced in the text. The camera exposure time was 20 ms.

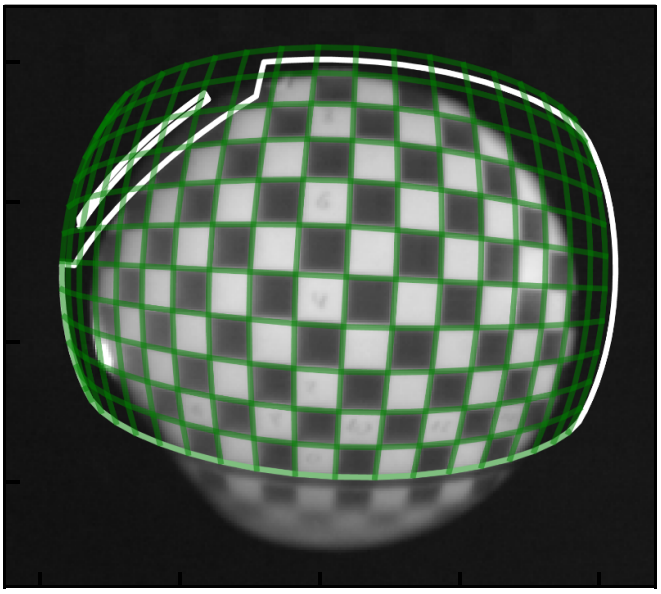

Figure 7. INPA calibration frame. A chess-pattern was placed in the scintillator plane. The scintillator and carbon foil contours are overlaid in white. In green, the chess-pattern generated with the calculated optical parameters.

first frames recorded in each discharge, when there is still no plasma.

During discharge #40259, the INPA shutter was opened and closed, allowing for a characterisation of the noise level due to light entering though the out-gassing holes. Figure 6 shows the mean number of counts in the INPA camera during this discharge. In the initial part of the discharge (indicated with a red dashed line in figure 6), with no FI source, is 4275 counts per pixel (from 65 000 of maximum in the camera). This is equivalent to ∼250 000 photons per second per pixel, considering the used exposure time (20 ms) and the camera quantum efficiency and electron multiplication factor. The noise in a phase with plasma but the shutter closed (indicated with a fuchsia dashed line), $t \sim 2.5$ in figure 6, is 4300 counts. This entails that only ∼25 counts are due to light entering through the out-gassing holes, and is therefore negligible. The noise during the phases with the shutter opened and no NBI#3 (indicated with a black dashed line) was measured at 4400 counts. This implies that the noise due to light entering the pinhole is around ∼100 counts. Note that in this last point, passive contribution is also included, see section 4.2 for more details. A *common* active INPA signal has around 35 000 counts at the peak, in this setup.

3.2. Scintillator to camera relation

In order to relate points in the scintillator with points in the camera sensor, a one parameter distortion model is applied:

$$\vec{r}_{\mathrm{CCD}}|_D = \vec{r}_c + (1+D)\,(\vec{r}_{\mathrm{CCD}} - \vec{r}_c) \tag{4}$$

where $\vec{r}_{\mathrm{CCD}}|_D$ is the distorted position in the camera sensor (in pixels), $\vec{r}_c$ is the position of the optical axis in the camera sensor (in pixels), and D and $\vec{r}_{\mathrm{CCD}}$ are respectively the distortion factor and the position in the absence of any distortion. The distortion factor is calculated as:

$$D = C|\vec{r}_{\mathrm{CCD}} - \vec{r}_c| \tag{5}$$

$$\vec{r}_{\mathrm{CCD}} = S \cdot \overleftrightarrow{R}\,(\alpha)\,\vec{r}_S + \vec{r}_0 \tag{6}$$

with C being the parameter to model the distortion magnitude, S the magnification factor at the optical axis (in px m^{-1}), $\overleftrightarrow{R}$ a rotation matrix to take into account the rotations of the image caused by the mirrors, $\vec{r}_S$ the position in the scintillator plate (in m) and $\vec{r}_0$ the position of the reference point of the scintillator in the camera. The constants C, α and S are estimated from the optical modelling and then fine tuned to fit the calibration images. These images were taken during the installation/post-campaign calibration of the detector. An example of a calibration image is shown in figure 7. The field-of-view does not include the corners of the scintillator, but no signal is expected in that region of the plate.

3.3. Carbon foil effect

The purpose of the carbon foil is the ionisation of CX neutrals. However, the carbon foil also produces attenuation, energy loss and scattering of the incident neutral flux. The carbon foil is supported by a 3 μm-thickness copper mesh. Neutral deuterium, hydrogen or alphas have a penetration range in the copper far below this thickness for energies below 100 keV [21], so any neutral impinging the copper mesh is stopped within it. The area blocked by the copper (according to the company data-sheet) is 39% of the foil area. SRIM [26] simulations suggest the scattering suffered by the neutrals while traversing

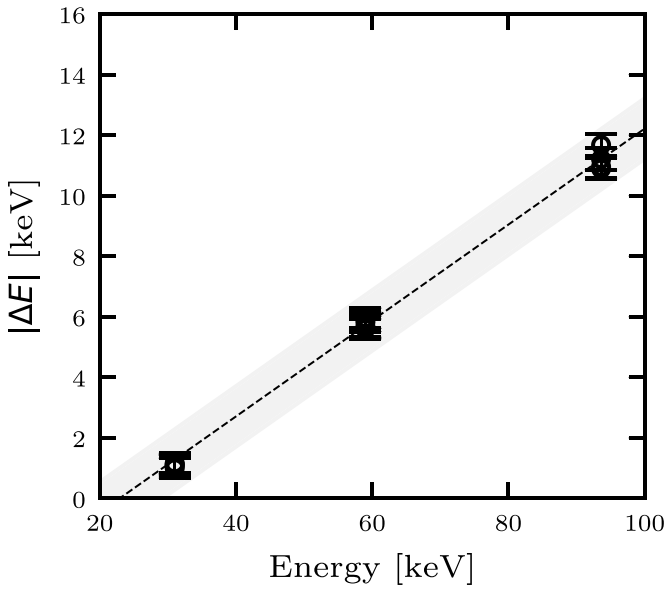

Figure 8. Energy loss in the carbon foil. Dots represent the energy loss measured from an on-axis FI distribution while the dashed line the fit included in the simulation code.

the carbon foil is negligible [21]. The energy loss and ionisation efficiency depend on the energy of the incident particle. The ionisation yield is assumed to follow the energy dependency presented in [21]. For the energy loss, data from MHD-quiescent phases were used to derive the energy loss. The energy of the recorded peak at the scintillator is compared with the nominal energy from the NBI injection. The measured energy loss is depicted in figure 8. The shaded area in figure 8 represents the uncertainty, which is assumed to come from the uncertainties in the thickness in the graphite foil. The latter are assumed to be around 10%, as reported at [21], which use a carbon foil from the same manufacturer. As can be observed, the energy loss align well with a linear dependency. This fitted linear dependency is included in the synthetic diagnostic.

3.4. *Finite focus and energy resolution*

Under ideal conditions, the energy resolution of the system for 93 keV deuterium ions is 5.1 keV (or 12 keV of FWHM assuming a Gaussian distribution) for −2.5 T magnetic field on axis [9]. This was calculated neglecting any spreading caused by differences in the energy loss due to thickness tolerance nor any optical non-ideality, such as limited camera pixel (px) size, finite focusing or distortion. To compare this value to the experimental energy resolution, a discharge with a MHD-quiescent phase where NBI#3 and #8 were active was taken as reference and the high energy peak of the signal was fitted to a Gaussian. To avoid taking the slowing down tail, only the portion above the injection energy was taken, as shown in figure 9(a). The result from the fits yields $\sigma_{\text{exp}} = 9.2 \pm 0.3$ keV. Part of the difference may be explained due to the electron temperature at the location of

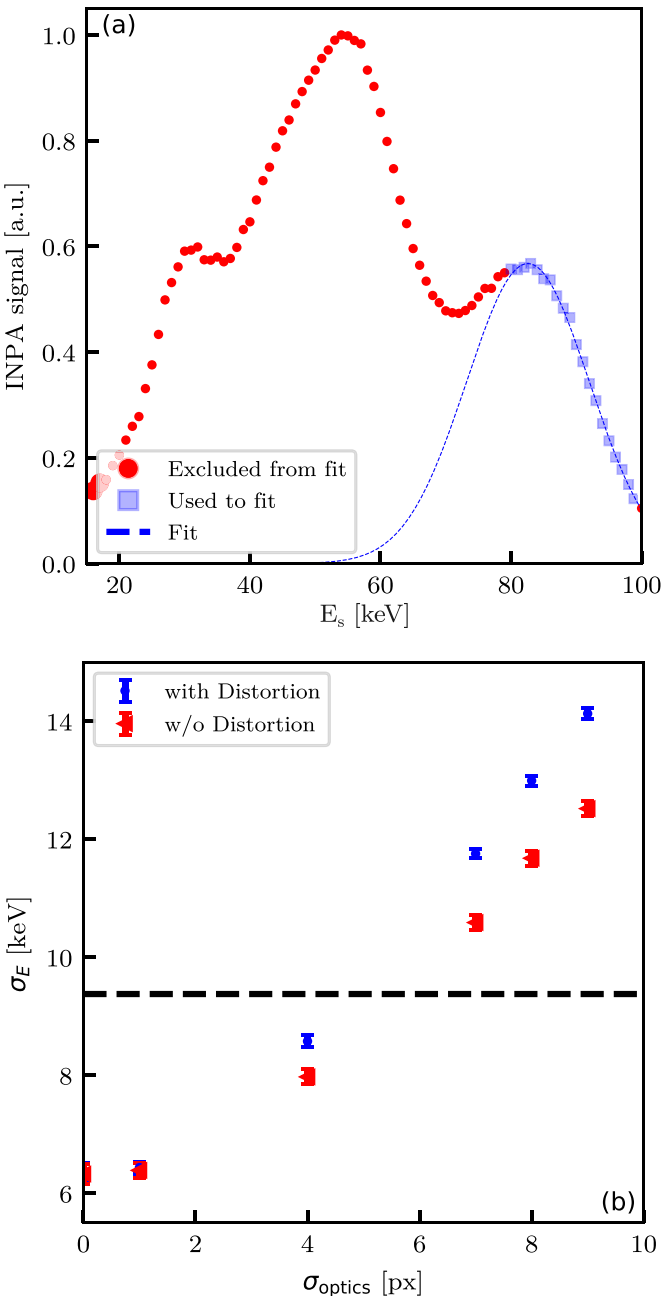

Figure 9. INPA energy resolution. (a) Fit to estimate the INPA energy resolution. Discharge #40415, $t = 6.86$ s. NBI#3 and NBI#8 were active. E_s represents the energy of the measured particles at the scintillator, after traversing the carbon foil. (b) Effect of optical resolution on the INPA energy resolution. Blue dots represent the calculation performed with the measured level of distortion, red triangles the case without any distortion. In both case, finite size of the camera pixel and 93 keV ions are considered. The horizontal dashed line represents the experimental energy resolution as estimated from discharge #40415.

the measurement (2 keV), which is known to broaden the FI distribution [7], the differences in energy loss in the foil caused by the uncertainties in foil thickness (∼1 keV assuming the foil thickness uncertainty as 10% and taking ∼10 keV as energy lost in the foil, as seen in the previous section) plus

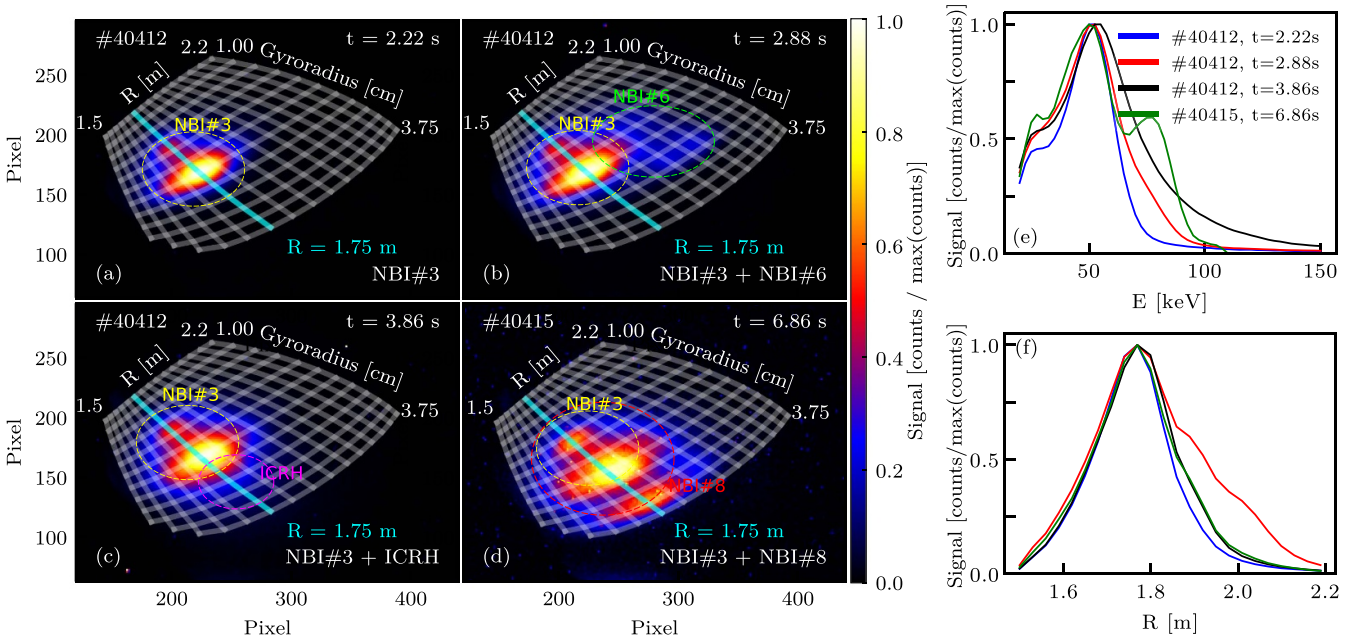

Figure 10. Examples of INPA signals. All frames where normalised to their maxima. The spacing in the R direction of the map is uniform (0.05 m) as well as in the gyroradius (energy) direction (0.25 cm). (a)–(c) Are taken at −2.5 T on axis, (d) at −2.0 T. $R = 1.75$, the approximate location of the magnetic axis, is highlighted in cyan. (a) Baseline scenario, contribution of NBI#3, the diagnostic active source of neutrals. (b) Measurement with off-axis NBI source. (c) Case where ICRH is activated. (d) Example of measurement with NBI#8 (AUG high energy on axis beam). (e) Integral of the signal along the radial direction, (f) integral of the signal along the energy direction.

the intrinsic uncertainty in the NBI energy (up to 1 keV for AUG). Combining quadratically these factors with the ideal energy resolution, the theoretical prediction would be 6.1 keV. The remaining difference can be attributed to the finite focus of the optical system, the finite pixel size and the optical distortion. In the optical design, σ_{px} (the number of pixels along which a signal coming from a point like source is distributed) was expected to be around 2 px. In figure 9(b), the energy resolution of the system is shown as a function of the optical resolution. According to the empirical energy resolution, the value of the optical resolution is 4.5. Another source of discrepancy could be a larger carbon foil scattering. Ultimately, this effect would be equivalent to the Gaussian spreading due to finite resolution of the optics and thus, is not considered here.

4. First INPA measurements at ASDEX Upgrade

4.1. INPA response to different FI distributions

To demonstrate the capability of the INPA diagnostic to capture the different FI distributions, different NBI sources and ion cyclotron resonant heating (ICRH) were used. An example of the obtained signals can be seen in figure 10, frames (a)–(c) correspond to a discharge with −2.5 T on axis while frame (d) corresponds to −2.0 T. All signals were normalised to the maximum of their peaks. Noise was subtracted averaging the first frames of the recording. Subplot (a) shows the signal for a case where only NBI#3 is switched on. As NBI#3 is the active source of neutrals for the diagnostic, this signal will be the baseline of the INPA diagnostic. The baseline signal is centred near the magnetic axis (located at $R = 1.75$ m in this discharge) and has two different energy components, corresponding to full and half energy components of the NBI. The third energy component is not noticeable due to a combination of factors: due to its lower energy it exhibits a larger reionisation of CX neutrals along the path towards the detector; and both the carbon foil ionisation efficiency and the scintillator yield are lower at lower energies [20, 21, 27]. This radial localisation is expected for NBI#3 as this beam creates on-axis FI distributions [13]. The gyroradius, r_l is here defined as:

$$r_l \equiv \frac{mv}{qB} \tag{7}$$

where m, v, and q are the mass, the velocity and the charge of the particle, respectively and B stands for the local magnetic field at the detector head. At the experiment magnetic field, the NBI#3 full injection energy (59 keV) corresponds to 2.5 cm. Figure 10(b) corresponds to a case where the off-axis beam, NBI#6, is activated, its fast ions are seen in the signal around 1.95 m and gyroradius 3.0 cm; at the experiment magnetic fields, this 3.0 cm corresponds to the full injection energy of NBI#6 (93 keV). Plot (c) shows the case where ICRH (36.5 MHz, which at the experiment magnetic field corresponds to the cyclotron frequency of H at 1.72 m, on-axis) is activated while NBI#3 was on. The shown signal is equivalent to the

frame (a) but a fast-ion tail towards larger gyroradii (higher energies) has formed, this can be better appreciated in subplot (e). The last camera frame corresponds to a case where NBI#8 was activated, this is an on-axis 93 keV beam source. The high energy peak is clearly visible, while the second and third energy components are mixed with the full and half energy components of NBI#3, due to the finite resolution of the system.

The ICRH population shown in figure 10(b) evolves with time, as the ICRH tail is built up. This temporal evolution is shown in detail in figure 11(a). As the time evolves, the population of ions with energies larger than the injection NBI#3 energy (59 keV) grows. This growth is shown in detail for ions with an energy of 120 keV (twice the injection energy), in figure 11(b), where the temporal variation of the signal at this energy relative to the signal at the NBI injection energy is depicted. The temporal evolution of this ratio, denoted here as γ, (for all energies above the injection one) can be fit to the relation:

$$\gamma = A\left(1 - \exp\left(-\frac{t - t_{\mathrm{ICRH}}}{\tau}\right)\right) \tag{8}$$

where $t - t_{\mathrm{ICRH}}$ represent the time from the onset of the ICRH and A and τ are the two parameters of the fit. Both A and τ are energy dependent. This constant τ measure the timescale on which the ICRH ion population stabilises via diffusion. The corresponding values of τ for each energy are depicted in figure 11(c) for two different ICRH phases, characterised by varying plasma density and temperature and, consequently, collisionality. The scaling of τ with different plasma parameters like density, temperature or Hydrogen concentration falls beyond the scope of this article and will be addressed in a follow-up publication.

4.2. Passive contribution

Thermal neutrals (mostly released by the wall) can contribute to the INPA signal, as they can penetrate the plasma and also undergo CX reactions with the FI. This signal is called *passive* contribution. Not accurate relationship can be established between the radial location of the FI and its velocity orientation. In the case of the AUG INPA diagnostic, the passive contribution is small and usually below the noise level, as the overlapping of the measurable fast-ion distribution and the edge neutral density is usually small, as observed for FIDA [13]. Only in low density discharges (line integrated density below $3 \cdot 10^{19}$ m^{-2}), where the penetration of thermal neutrals is larger, this signal could be observed. An example frame of the passive signal in this low density discharge is shown in figure 12. Notice that this signal has a maximum of 500 counts ($\sim$25 000 photons per second and per pixel) in the camera signal while the active signal for this same shot in a later phase of the discharge, has a maximum of 20 000 counts, so this passive contribution is less than 5%.

4.3. Evolution of INPA signal during a discharge

Both density and temperature strongly affect the INPA signal. As the density increases, beam penetration is reduced and signal loss due to re-ionisation of the CX neutrals increases; both factors depend exponentially on the density. Also, when increasing the density, the collisionallity increases and hence the FI slowing down time decreases, reducing further the INPA signal. With respect to the temperature, its effect is also twofold, on the one hand the CX reactivity changes with temperature [22] and on the other hand, larger temperatures imply a larger FI slowing down time and hence a larger FI content in the plasma, so more signal. From both effects, the latter dominates, as FI have velocities well above the thermal plasma, so changes in temperatures do not imply larger changes in the relative velocities between FI and thermal ions and hence, in the reactivity. This general trend can be seen in figure 13, where the signal for a -2.5 T discharge is represented, along with the plasma density, temperature and the NBI time trace. Between 1.2 and 2.2 s, when the density is fairly constant, the INPA signal follows the plasma temperature, and it decreases in the phases when density is increasing, as expected. Notice that up to $n_e(\mathrm{core}) \sim 8 \cdot 10^{19}\mathrm{m}^{-3}$ the active signal can be seen.

To demonstrate the effect of these variables in the INPA signal, three consecutive shots were performed keeping similar plasma shape while scanning density and temperature via current and heating scans. The INPA signal was integrated in energy from 48 to 65 keV and in radius from 1.70 to 1.85 m in temporal windows of 20 ms where only NBI#3 was switched on as on-axis source. This restricted range was selected to isolate just the peak originating from the main injection energy of NBI#3. This integral is represented in figure 14 against the electron collisionality at the core ($\rho = 0.25$), calculated as in [28]:

$$\nu_e^* = 0.0012 \frac{q R_0 Z_{\mathrm{eff}} n_e \left[10^{19}\,\mathrm{m}^{-3}\right]}{\epsilon^{3/2}\left(T_e\ [\mathrm{keV}]\right)^2} \tag{9}$$

where q is the safety factor, R_0 the magnetic axis position, Z_{eff} the effective charge, n_e the electron density, ε the aspect ratio and T_e the electron temperature; and all profile quantities are evaluated at the core ($\rho \sim 0.25$). As the collisionality increases the INPA signal decreases. The spreading in the figure can be attributed to the different profile shape at each time point as well as the presence of some MHD fluctuation which causes FI redistribution.

5. Synthetic diagnostic and analysis tool

The INPA synthetic signal is calculated using the CX flux obtained by the FIDASIM code [22, 29, 30] and a particle tracker which includes the effects on the carbon foil and scintillator emission, INPASIM [9]. The INPASIM code was upgraded with a Boris leap-frog algorithm [31] to track the

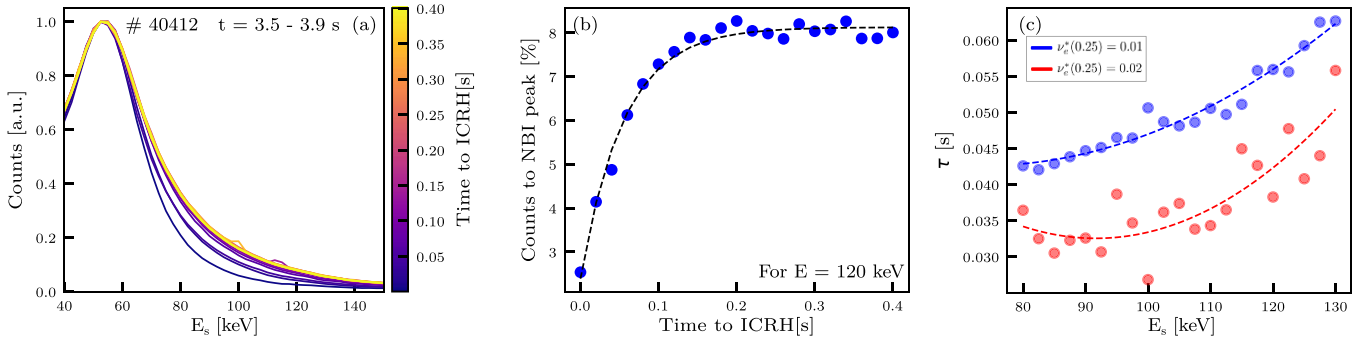

Figure 11. Evolution of the ICRH population. (a) Temporal evolution of the measured energy profile (normalised to the signal at the NBI injection energy). (b) Temporal evolution of the ratio of the signal at 120 keV respect to the signal at the NBI injection energy. (c) Fitted constant τ for each energy, in blue the results for the first ICRH phase, between 3.5 and 3.9 s, in red the results for the second ICRH phase, between 5.6 and 6.0 s. A parabolic fit was added to guide the eye. Discharge #40412.

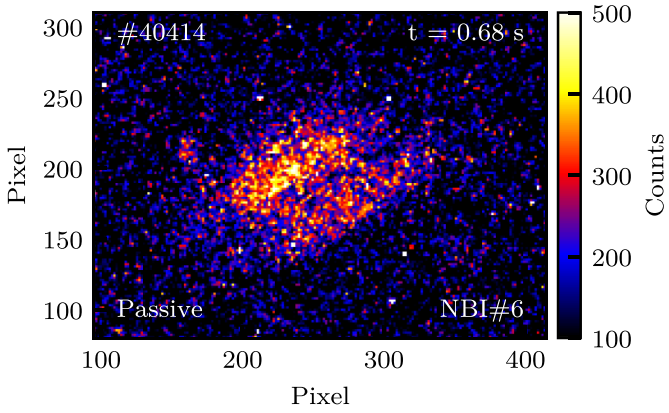

Figure 12. Example of passive signal of INPA. Discharge #40414, $t = 0.68$ s, off-axis NBI#6 injection.

markers inside the detector head, the possibility to include any 3D geometry via *.stl* files and the inclusion of electric fields. It was also combined with the already existing FILDSIM code [32]. Full details of the upgraded code are out of the scope of this publication and will be presented in a future article together with the first tomographic inversions of INPA signals.

5.1. Spatial localisation and multiple NBI impact

The radial resolution mainly depends on the extension of the source of neutrals along the radial direction and the field of view of the INPA diagnostic. Due to the dependence on the neutral source, it can not be directly estimated from diagnostic measurements but needs to be calculated via simulation, comparing the ionisation position of the CX particles with the reconstructed position at the scintillator, yielding values of $\sigma < 3.0$ cm at the low field side [9], including just 1 NBI as neutral source. Activating several NBI sources can produce a degradation of the radial resolution. Nonetheless, the field of view of INPA is constrained enough so other beam sources have a small contribution, as depicted in figures 15 and 16.

In figure 15, the contours of the NBI deposition are represented together with the birth position of CX neutrals, for the case of an on-axis distribution function. Notice that even if the neutral distribution significantly differs, the actual birth position of the signal, does not shift significantly nor does it become wider. This is due to the INPA field-of-view. This effect can be seen in more detail in figure 16, where the distribution of markers which fall into the strike map position $R = 1.80$ m is plotted for the case of the different NBI configurations. As can be observed, there are no significant changes, only a shift smaller than a cm when the NBI#4 is also active. Hence, the activation of other beams from box 1 does not hamper the INPA operation and does not degrade its resolution significantly.

5.2. Monte-Carlo technique to remap the signal

As for FILD diagnostics, the FILDSIM code allows to launch Monte Carlo (MC) markers at the detector pinhole with given energy and which come from a given radial position along the NBI line. Due to the finite collimator and pinhole sizes these markers with similar energy and radial birth location can strike in different points along the scintillator, which are then transported to different points along the camera sensor. Let $D(x_1,x_2|E,R)$ be the distribution of markers on the camera sensor (defined by the variables x_1, x_2) conditioned on the marker energy E and radial birth location R. A mapping exist which relate the 2D camera space (x_1,x_2) with the 2D phase space E,R this map is defined by the two functions [33]:

$$\psi_E : \mathbb{E}_{D(x_1,x_2|E,R)}\,(x_1,x_2) \rightarrow E \tag{10}$$

$$\psi_R : \mathbb{E}_{D(x_1,x_2|E,R)}\,(x_1,x_2) \rightarrow R \tag{11}$$

in this mapping the centre of mass of the strike points distribution $D(x_1,x_2|E,R)$ correspond to the point (E,R). This one to one mapping is the so called *strike map* [32].

The *strike map* can be used to translate the camera signal, which is a distribution of counts per pixels, into a gyroradius (energy) - major radius distribution. To this end, also a MC

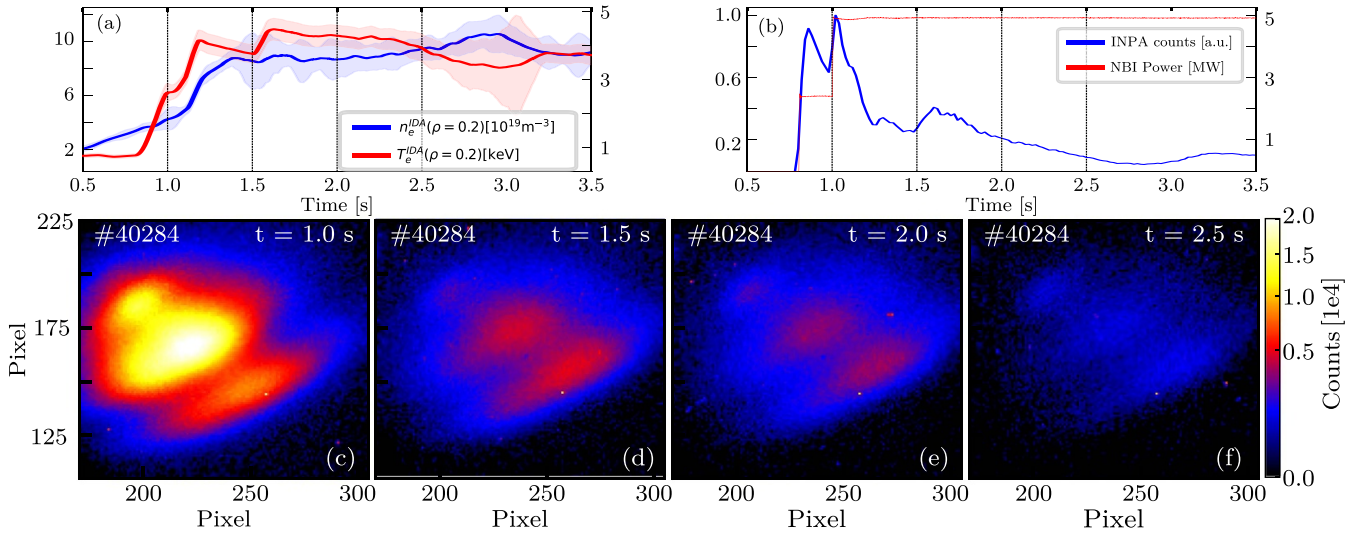

Figure 13. Evolution of the INPA signal during a *typical* −2.5 T discharge. (a) Density (left axis) and temperature (right axis) taken at $\rho = 0.2$, shaded areas represent the confidence interval. (b) INPA signal (left axis), integral of the camera frame over the scintillator, and NBI timetraces (right axis). (c)–(f) Regions or interest where NBI signal is registered in the camera.

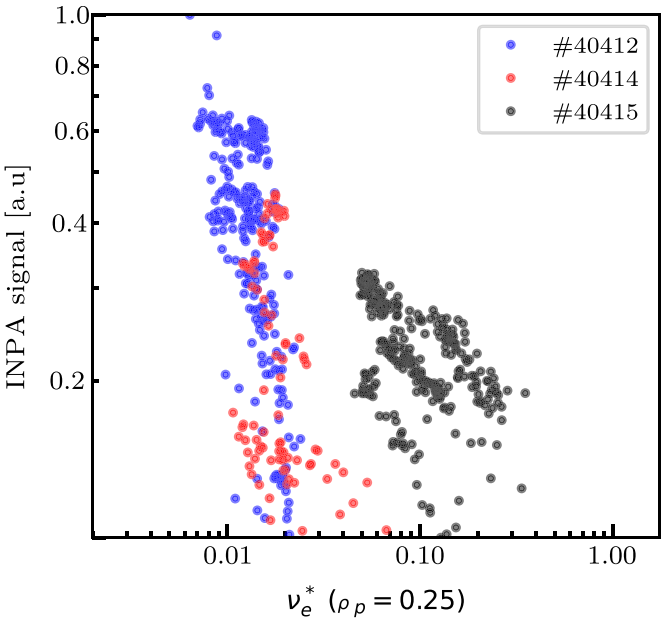

Figure 14. INPA signal versus electron collisionality at the core for different shots. Each point correspond to an integration time of 20 ms. All signals where normalise to the maximum signal of shot #40412.

approach is used. The signal for each pixel, S_{ij}, is written as a collection of MC markers as:

$$S_{ij} = \frac{C_{ij}}{N}\sum_{k=1}^{N}\delta\left(x_1 - x_1^k, x_2 - x_2^k\right) \tag{12}$$

where C_{ij} is the total number of counts in the camera pixel (i,j), N the number of launched MC markers, and (x_1^k, x_2^k) the position of the marker, which is selected randomly along the pixel size via an uniform distribution. Employing the strike map, this distribution along the pixel is directly transformed to the phase space:

$$S_{ij}(E,R) = \frac{C_{ij}}{N}\sum_{k=1}^{N}\delta\left(E - \psi_E\left(x_1^k, x_2^k\right), R - \psi_R\left(x_1^k, x_2^k\right)\right) \tag{13}$$

from which the total signal per volume of the phase space can be written as:

$$\begin{aligned} S(E,R) &= \sum_{i,j} S_{ij}(E,R) \\ &= \sum_{i,j}\frac{C_{ij}}{N}\sum_{k=1}^{N}\delta\left(E - \psi_E\left(x_1^k, x_2^k\right), R - \psi_R\left(x_1^k, x_2^k\right)\right). \end{aligned} \tag{14}$$

If the process is done for a series of *delta like* camera frames, ie ideal camera frames such that $S_{ij} = 0$ for all (i,j) except one pixel of the camera, the phase space covered by that particular pixel can be determine. Using this information, is direct to define a 4D matrix, $T^{ij}_{\alpha\beta}$, the *translation matrix*, such that:

$$S_{\alpha\beta} = T^{ij}_{\alpha\beta} S_{ij} \tag{15}$$

where $S_{\alpha\beta}$ is the signal per unit of gyroradius (energy) and major radius (the discretisation on an uniform grid of $S(E,R)$ from equation (14)), S_{ij} is the camera frame and $\alpha\beta$ run over the gyroradius-radius space while ij over the pixels. Einstein summation criteria is assumed. These matrices can be pre-computed and stored for each strike map, reducing the problem

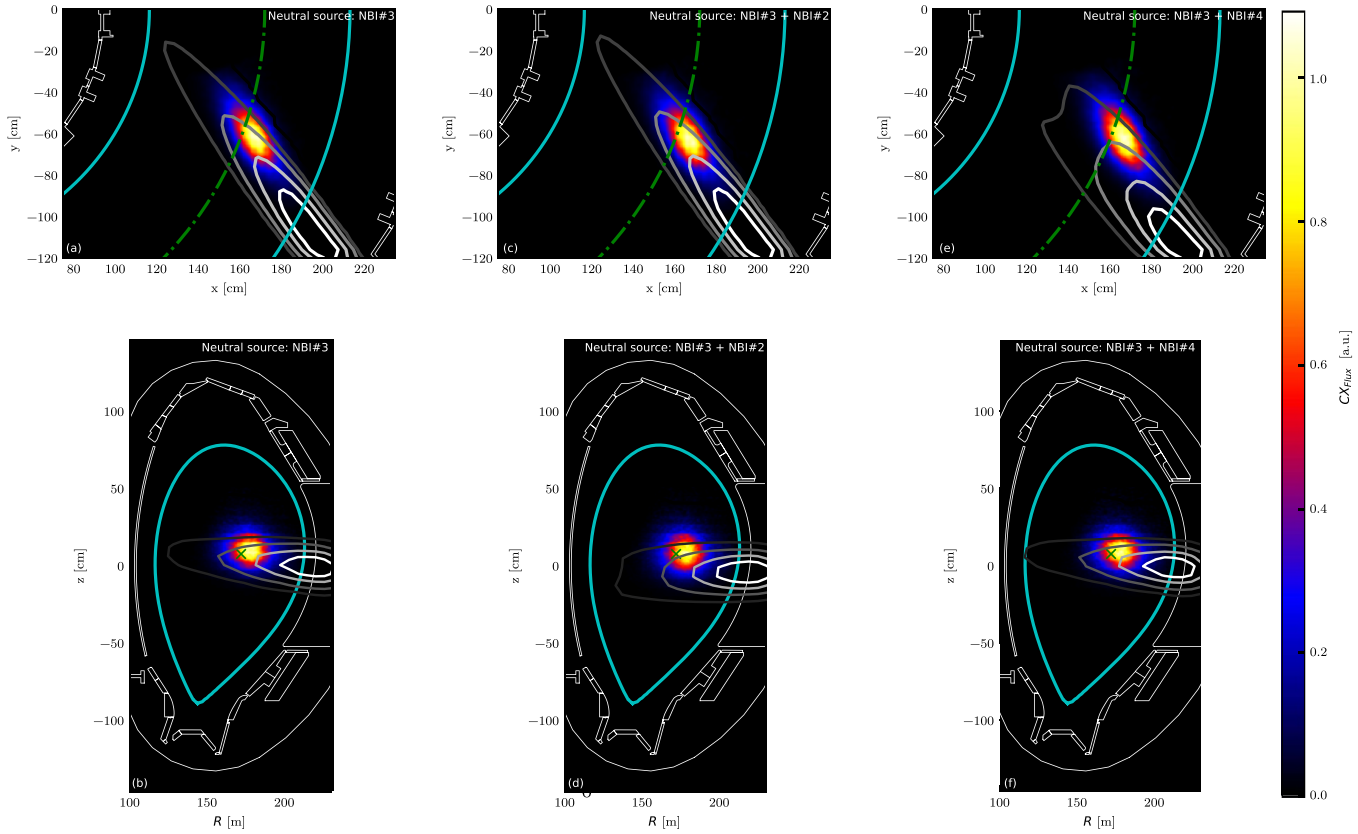

Figure 15. Simulated birth position of the INPA signal and NBI deposition. Coloured contours represent birth location of the neutrals measured at INPA. Grey scaled lines represent the density of NBI neutrals (the whitest line represents the contours of 75% of the maxima value and the darker one represents the 25%). Green line (cross) indicates the magnetic axis and cyan lines the separatrix. (a) and (b) subplot represent the simulation using only NBI#3, (c) and (d) the case of NBI#3 and NBI#2 while (e) and (f) the case of NBI#3 and #4. All cases were normalised to their respective maxima.

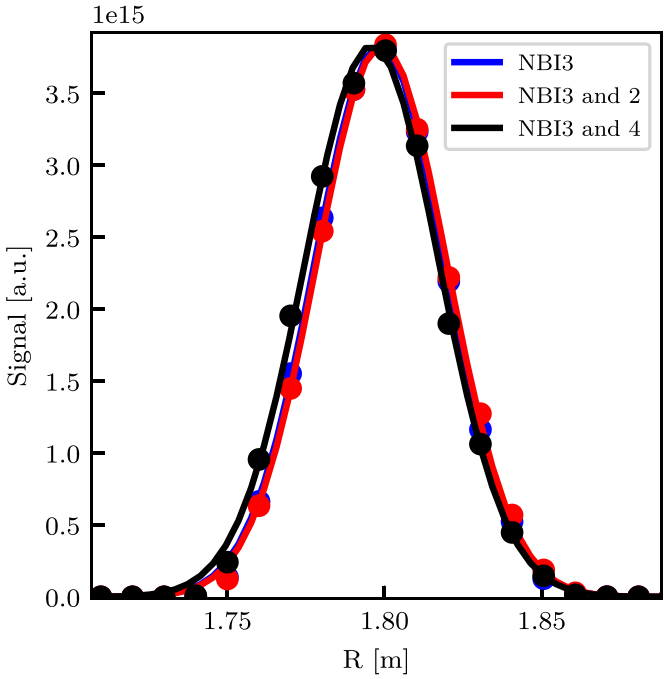

Figure 16. Radial resolution of the INPA diagnostic. Distribution of birth radial position arriving to the strike map position related with $R = 1.80$ m. Dots represent the simulation data, while the solid line represent the performed fit to estimate the resolution.

of transforming from the camera space to the phase space to a simple product of matrices.

5.3. Absolute calibration of the synthetic diagnostic

The FIDASIM code provides as output the absolute neutral flux reaching the carbon foil of INPA (in particles per second), therefore, a direct comparison can be established with the experimental data:

$$C/\tau = \Phi_{\mathrm{FIDASIM}} \cdot G * Y_{\mathrm{Foil}} \cdot Y_{\mathrm{Scint}} \cdot T_{\Omega} \cdot R \cdot QE \cdot \alpha \cdot$$
$$F \equiv \xi\, \Phi_{\mathrm{FIDASIM}} \tag{16}$$

where C is the INPA signal in counts, τ the camera integration time, Φ_{FIDASIM} is the neutral in-flux calculated with FIDASIM, G is the area of the foil not blocked by the support copper mesh, Y_{Foil} the ionisation efficiency on the foil, Y_{Scint} the photons emitted by the scintillator per each incident ion, T_{Ω} the geometric collection efficiency of the optics, R the transmission efficiency of the optical system, QE the camera quantum efficiency at the scintillator emission wavelength, α the number of counts per incident electron in the chip, F the digital multiplication factor and ξ is just the overall product of all the factors except the FIDASIM flux. Notice that Y_{Foil} and Y_{Scint} are a function of the particle energy, hence ξ depends on energy. The former can be estimated as presented in [21] while the latter can be extrapolated from the measurements performed in [6, 27]. The values of all factors are detailed in table 1: G is taken from the foil data-sheet, Y_{Foil} from the data presented in [21], Y_{Scint} is calculated using the Birk model for normal incidence [27], T_{Ω} and R are taken from the optical design, QE and α are taken from the camera data-sheet and F is 16, as imposed in the acquisition software of the CCD camera. ξ as a function of energy is shown in figure 17 for the case of a time point in discharge #40284. The error bars come from the uncertainties in the predicted Φ_{FIDASIM} due to density profile uncertainties. This density profile was taken from Integrated Data Analysis (IDA), a probabilistic tool for coherent combination of heterogeneous diagnostics at AUG [34]. Notice that the measured ξ is in the range of $3 \cdot 10^{-4}$ camera counts per neutral while the rough estimation (for 45 keV) is $\xi = 0.0072$ camera counts per neutral, as indicated in table 1. The reason from the overall discrepancy may be found mainly in the scintillator yield as it is an extrapolation from measurements taken at the MeV range of energies done with normal beam incidence. Recent measurements probe this extrapolation over-predict the photon yield in the keV range [35]. Unfortunately, complete energy dependency of the scintillator yield of the used powder at the complete energy range and different incidents angles are not available. This measurements are planned for the near future. Regardless of the overall factor, it is expected that both the foil and scintillator yield can be approximated by a linear function in the relatively small range of NBI energies, so the expected energy trend is parabolic. The parabolic fitting can be seen in dashed lines in the figure 17. This fit has later been applied to scale the synthetic signals.

Table 1. INPA absolute transmission factors.

Factor	Value
G	0.6
Y_{Foil}(45 keV)	0.33 Ions/Neutral
Y_{Scint}(45 keV)	3500 Photons/Ion
T_{Ω}	$1.8 \cdot 10^{-5}$
R	0.75
QE	0.35 Electrons/Photon
α	1/6.5 Counts/Electron
F	16
ξ(45 keV)	0.0072 Counts/Neutral

A comparison of the synthetic and measured signals for the case of an on-axis NBI distribution during a MHD-quiescent phase is shown in figure 18 for discharge #40284. The neoclassical fast-ion distribution function calculated by TRANSP was used for the calculation of the synthetic signal. Subplot (a) shows the comparison between the measured and simulated energy distribution and subplot (b) compares the radial ones. In the simulation, the parabolic fit shown previously was applied. Both simulation and experiments agree within the uncertainty. Notice that the agreement is worse for the case of the radial profile in the region near $R = 2$ m, where the simulation over-predicts. The reason for this is under investigation.

When the off-axis beam is added on top of the on-axis (diagnostic) beam, neoclassical predictions fails to reproduce the synthetic signal, as can be appreciated in figure 18(d). A 0.1 $\mathrm{m}^2\,\mathrm{s}^{-1}$ diffusion for the fast-ions was introduced in NUBEAM (TRANSP), in the interval $\rho_t \epsilon (0.35, 0.55)$ and zero elsewhere. This small anomalous diffusion coefficient is in line with previous AUG studies and can be associated with turbulent fluctuations correlated with thermal transport as explored in [2] or due to the low amplitude mode $n = 3$, $m = 2$ mode which develops when adding the second NBI (see figure 19). The precise reason behind this redistribution is currently being studied and out of the scope of this article. It will be addressed in a future publication. The comparison of INPA signal with the predictions for with the inclusion of diffusion can be seen in figures 18(c) and (d). With the inclusion of the off-axis diffusion, an agreement inside error bars is found between simulations and experiment. For FIDA, an improvement in the agreement is also found when including diffusion, as shown in figure 20. Notice that the effect of the diffusion is smaller in the FIDA signal than in the INPA one. This is due to the fact that the INPA explores a narrow pitch region while FIDA integrates over a wide region of the velocity space.

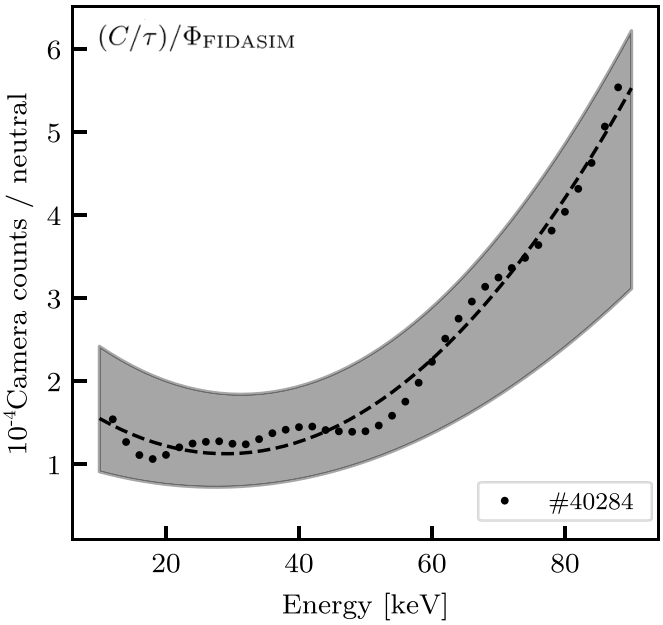

Figure 17. Comparison of synthetic and experimental energy profiles. Ratio between the counts per second in the INPA camera (C/τ) and the number of neutrals per second arriving to the foil predicted by FIDASIM (Φ_{FIDASIM}), ξ from equation (16). Dashed line represents the parabolic fits implemented in the code while the shaded area represents the confidence interval of those fits, when including a variation in the density profile of the order of IDA uncertainty.

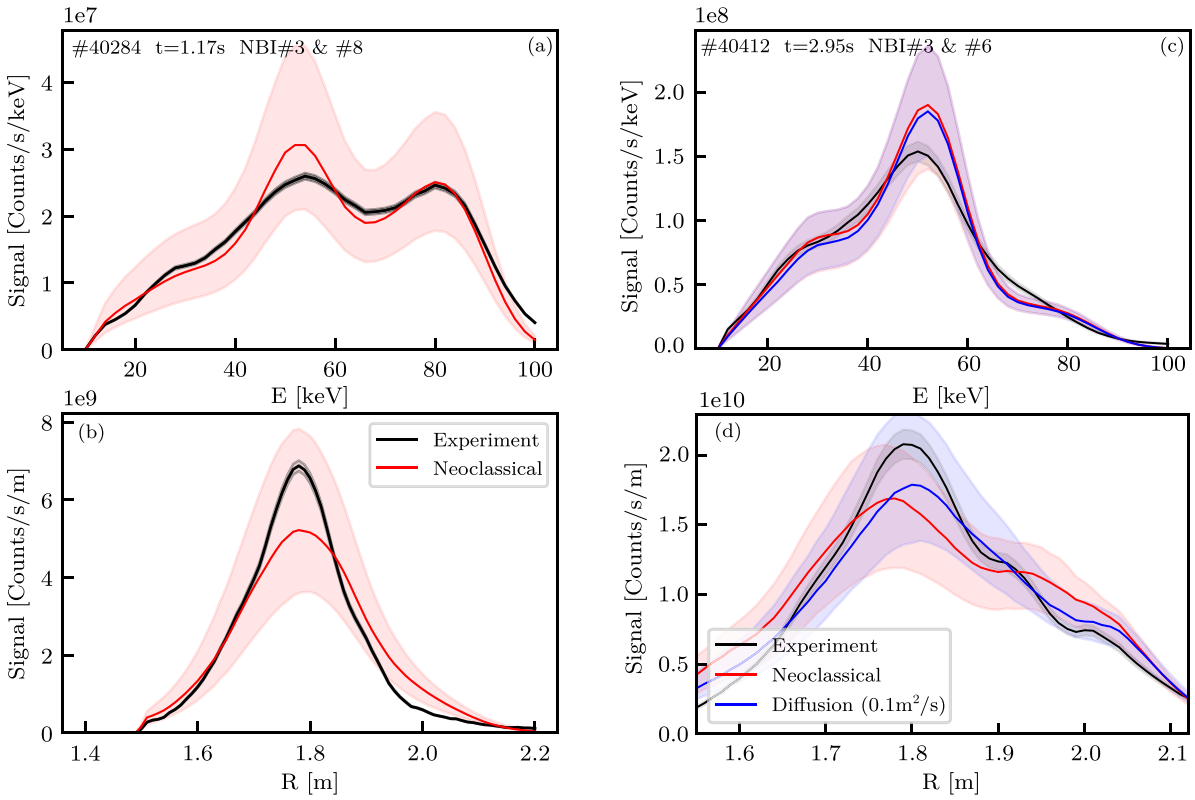

Figure 18. Comparison of synthetic and experimental INPA signals. (a) and (b) #40284 and time 1.17 s, only NBI#3 and 8 were active. Shaded areas represent the uncertainty: for the simulations, estimated repeating it with a density varied inside the confidence interval from IDA, for the measurement, the ∼2% coming from optical calibration. (c) and (d) Equivalent for #40412 and time 2.95 s, only NBI#3 and 6 were active.

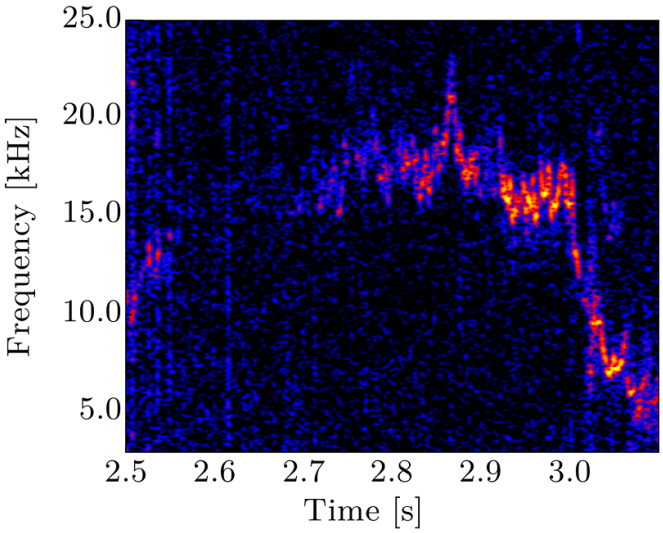

Figure 19. Spectrogram from ECE diagnostic during the phase of combined on- and off-axis NBI injection. An $n = 3$, $m = 2$ mode develops. Discharge #40412.

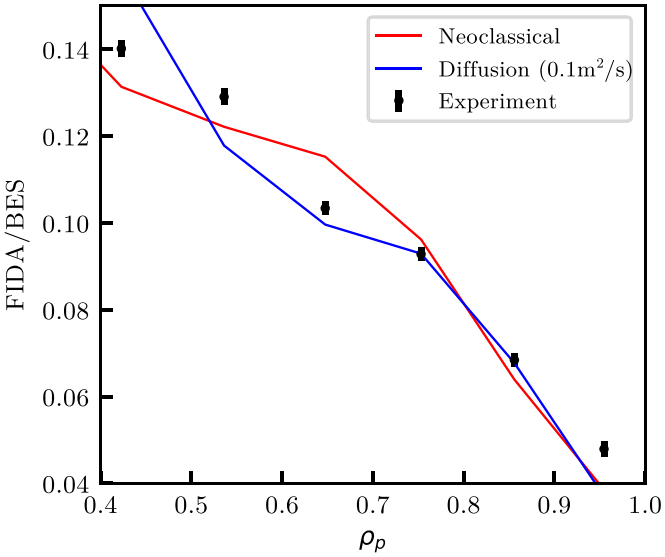

Figure 20. Comparison of synthetic and experimental FIDA/BES signals. #40412 and time 2.95 s, only NBI#3 and 6 were active.

The agreement between the experimental and synthetic signals is maintained across varying plasma electron temperatures and densities. In order to visualise this, during a time range in which both plasma density and temperatures undergo changes (up to 15% for plasma density and 20% for temperature), the experimental and synthetic signals are integrated within a region close to the magnetic axis at the injection energy of NBI#3. These integrated signals are then normalised to the signal at the beginning of the time range. The comparison is illustrated in figure 21. With the exception of a minor dispersion, likely attributed to the use of a constant effective charge in the simulation throughout the entire time range, the synthetic and experimental signals agree.

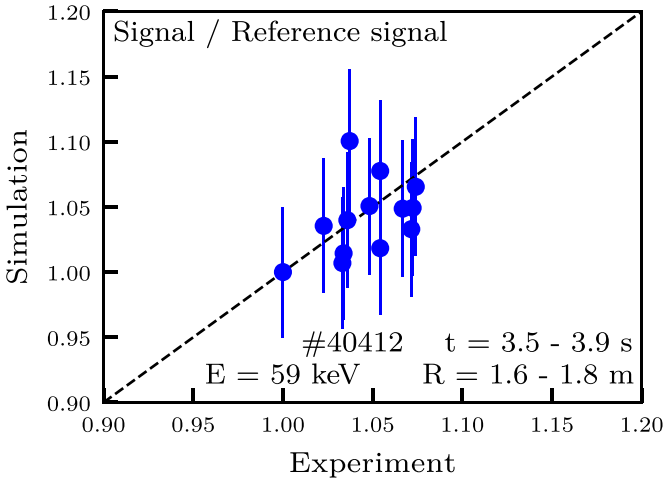

Figure 21. Changes in experimental and synthetic signal due to changes in plasma temperature and density. The x and y axis represent the signal at the different time points, integrated near the magnetic axis and at the NBI#3 injection energy, normalised to the signal at the beginning of the time range. The dashed line represent the ideal behaviour $y = x$.

6. Conclusions

An Imaging Neutral Particle Analyser (INPA) diagnostic has been installed and commissioned at the ASDEX Upgrade (AUG) tokamak. It has been demonstrated that the detector is sensitive to on/off-axis NBI distribution as well as ICRH FI distributions. The diagnostic features a resolution of 9 keV and 3 cm (one sigma) for full energy (93 keV) NBI ions. Due to its field of view, this resolution is not hampered if additional NBI sources from the same NBI box are switched on.

The signal level decreases strongly with collisionality, as expected; nonetheless, good signal to noise ratio can be achieved up to $n_e(0) \sim 8 \cdot 10^{19}$ m^{-3} with an integration time of 20 ms.

The synthetic diagnostic and analysis tools were upgraded, achieving a significant improvement in the execution time and implementing a MC approach to mitigate the effect of the finite size of the camera pixel. The validation of this synthetic diagnostic was successfully carried out during MHD quiescent phases. Apart from an overall factor of 16, most probably coming from the extrapolation of the scintillator yield measurements, good agreement was found.

Data availability statement

The data cannot be made publicly available upon publication because they are not available in a format that is sufficiently accessible or reusable by other researchers. The data that support the findings of this study are available upon reasonable request from the authors.

Acknowledgments

The authors would like to thank all technicians from the AUG team, who helped in the construction and installation of the

detector. In particular to Herr Wolfgang Popken and Herr Wolfgang Zeidner for their many hours of help and support.

This project received funding from the European Research Council (ERC) under the European Union's Horizon 2020 research and innovation program (Grant Agreement No. 805162) and the Spanish Ministerio de Ciencia, Innovación y Universidades (Grant No. FPU19/02486). J Galdon-Quiroga acknowledges support by the European Union under the Marie Sklodowska Curie Grant Agreement No. 101069021.

ORCID iDs

J Rueda-Rueda https://orcid.org/0000-0002-4535-326X
M Garcia-Munoz https://orcid.org/0000-0002-3241-502X
E Viezzer https://orcid.org/0000-0001-6419-6848
P A Schneider https://orcid.org/0000-0001-7257-3412
J Garcia-Dominguez https://orcid.org/0000-0002-3903-0560
P Oyola https://orcid.org/0000-0002-8455-1090
J Galdon-Quiroga https://orcid.org/0000-0002-7415-1894
J Hidalgo-Salaverri https://orcid.org/0000-0002-3008-0393
X Du https://orcid.org/0000-0001-6127-2825
M A Van Zeeland https://orcid.org/0000-0002-7911-2739
M Videla-Trevin https://orcid.org/0000-0002-7218-0392
A Jansen van Vuuren https://orcid.org/0000-0003-1732-3642

References

[1] Pinches S D *et al* (JET-EFDA Contributors) 2004 *Plasma Phys. Control. Fusion* **46** B187
[2] Günter S *et al* (ASDEX Upgrade Team) 2007 *Nucl. Fusion* **47** 025
[3] García-Muñoz M, Martin P, Fahrbach H-U, Gobbin M, Günter S, Maraschek M, Marrelli L and Zohm H (The ASDEX Upgrade Team) 2007 *Nucl. Fusion* **47** L10
[4] Sharapov S *et al* (JET Team) 2000 *Nucl. Fusion* **40** 1363
[5] White R B, Fredrickson E, Darrow D, Zarnstorff M, Wilson R, Zweben S, Hill K, Chen Y and Fu G 1995 *Phys. Plasmas* **2** 2871
[6] Galdon-Quiroga J *et al* 2018 *Nucl. Fusion* **58** 036005
[7] Heidbrink W W and Sadler G J 1994 *Nucl. Fusion* **34** 535
[8] Du X, Heidbrink W, Zeeland M V, Gonzalez-Martin J, Austin M, Yan Z and McKee G 2023 *Nucl. Fusion* **63** 046020
[9] Rueda-Rueda J *et al* (ASDEX Upgrade Team) 2021 *Rev. Sci. Instrum.* **92** 043554
[10] Garcia-Dominguez J, Rueda-Rueda J, Viezzer E, Schneider P A, Ayllon-Guerola J, Garcia-Munoz M, Hidalgo-Salaverri J, Mancini A, Videla M and Herrmann A 2022 *IEEE Trans. Plasma Sci.* **50** 4138
[11] García-Muñoz M, Fahrbach H U and Zohm H 2009 *Rev. Sci. Instrum.* **80** 053503
[12] Koleva M, Tardini G, Zohm H, Äkäslompolo S and Leppänen J (The ASDEX Upgrade Team) 2021 *Fusion Eng. Des.* **170** 112702
[13] Geiger B, Garcia-Munoz M, Heidbrink W W, McDermott R M, Tardini G, Dux R, Fischer R and Igochine V (ASDEX Upgrade Team) 2011 *Plasma Phys. Control. Fusion* **53** 065010
[14] Schneider P A, Blank H, Geiger B, Mank K, Martinov S, Ryter F, Weiland M and Weller A 2015 *Rev. Sci. Instrum.* **86** 073508
[15] Ochoukov R *et al* 2018 *Rev. Sci. Instrum.* **89** 10J101
[16] Korsholm S, Bindslev H, Furtula V, Leipold F, Meo F, Michelsen P, Moseev D, Nielsen S, Salewski M and Stejner M 2010 *Nucl. Instrum. Methods Phys. Res.* A **623** 677
[17] Hutchinson I H 2002 *Principles of Plasma Diagnostics* 2nd edn (Cambridge University Press)
[18] Heidbrink W W, Liu D, Luo Y, Ruskov E and Geiger B 2011 *Commun. Comput. Phys.* **10** 716
[19] Medley S S, Donné A J, Kaita R, Kislyakov A I, Petrov M P and Roquemore A L 2008 *Rev. Sci. Instrum.* **79** 1
[20] Du X, Van Zeeland M, Heidbrink W and Su D 2018 *Nucl. Fusion* **58** 082006
[21] Du X, Zeeland M V, Heidbrink W, Stagner L, Wingen A, Lin D and Collins C 2020 *Nucl. Fusion* **60** 112001
[22] Geiger B 2012 Fast-ion transport studies using FIDA spectroscopy at the ASDEX Upgrade tokamak *PhD Thesis* Ludwig-Maximilians-Universität München
[23] van Vuuren A J, Geiger B, Schneider P, Bogar K, Poloskei P, Cathey A, Hoelzl M, Jacobsen A, Cavedon M and Dux R (The ASDEX Upgrade Team) 2021 *Nucl. Fusion* **61** 046001
[24] Breslau J *et al* 2018 *TRANSP Code* (https://doi.org/10.11578/dc.20180627.4)
[25] Hawryluk R 1981 *Physics of Plasmas Close to Thermonuclear Conditions* (Pergamon) p 19
[26] Ziegler J 1983 *SRIM* (available at: www.srim.org/)
[27] Rodríguez M 2017 *PhD Thesis* TFG, Seville
[28] Sauter O, Angioni C and Lin-Liu Y R 1999 *Phys. Plasmas* **6** 2834
[29] Geiger B *et al* 2020 *Plasma Phys. Control. Fusion* **62** 105008
[30] Stagner L, Geiger B and Heidbrink W 2020 FIDASIM: a neutral beam and fast-ion diagnostic modeling suite (https://doi.org/10.5281/zenodo.1341369)
[31] Naval Research Laboratory (ed) 1970 *Proc. 4th Conf. on Numerical Simulation of Plasmas* (Naval Research Laboratory) pp 3–67
[32] Galdon-Quiroga J *et al* 2018 *Plasma Phys. Control. Fusion* **60** 105005
[33] Schmidt Bo S 2024 A new FILDSIM model for improved velocity-space sensitivity modelling and reconstructions *Plasma Phys. Control. Fusion* submitted
[34] Fischer R, Fuchs C J, Kurzan B, Suttrop W and Wolfrum E (ASDEX Upgrade Team) 2010 *Fusion Sci. Technol.* **58** 675
[35] Dominguez J A V 2019 Caracterización de materiales centelleadores para dispositivos de fusión usando haces de iones negativos *Master Thesis* University of Seville (available at: https://idus.us.es/handle/11441/94314)